

Parametric Reduced-Order Models for Probabilistic Analysis of Unsteady Aerodynamic Applications

T. Bui-Thanh* and K. Willcox†

Massachusetts Institute of Technology, Cambridge, Massachusetts 02139

and

O. Ghattas‡

University of Texas at Austin, Austin, Texas 78712

DOI: 10.2514/1.35850

We address the problem of propagating input uncertainties through a computational fluid dynamics model. Methods such as Monte Carlo simulation can require many thousands (or more) of computational fluid dynamics solves, rendering them prohibitively expensive for practical applications. This expense can be overcome with reduced-order models that preserve the essential flow dynamics. The specific contributions of this paper are as follows: first, to derive a linearized computational fluid dynamics model that permits the effects of geometry variations to be represented with an explicit affine function; second, to propose an adaptive sampling method to derive a reduced basis that is effective over the joint probability density of the geometry input parameters. The method is applied to derive efficient reduced models for probabilistic analysis of a two-dimensional problem governed by the linearized Euler equations. Reduced-order models that achieve 3-orders-of-magnitude reduction in the number of states are shown to accurately reproduce computational fluid dynamics Monte Carlo simulation results at a fraction of the computational cost.

Nomenclature

| | | |
|--------------------|---|---|
| \mathbf{A} | = | Jacobian matrix |
| \mathbf{A}_r | = | Reduced Jacobian matrix |
| \mathbf{A}_0 | = | Jacobian matrix corresponding to the average geometry |
| \mathbf{B} | = | input matrix |
| \mathbf{B}_r | = | reduced input matrix |
| \mathbf{B}_0 | = | input matrix corresponding to the average geometry |
| \mathbf{C} | = | output matrix |
| \mathbf{C}_r | = | reduced output matrix |
| \mathbf{C}_0 | = | output matrix corresponding to the average geometry |
| \mathbf{E} | = | mass matrix |
| \mathbf{E}_r | = | reduced mass matrix |
| \mathbf{E}_0 | = | mass matrix corresponding to the average geometry |
| \mathcal{G} | = | cost functional |
| \mathbf{g} | = | geometry vector |
| $\bar{\mathbf{g}}$ | = | average geometric variation |
| \mathbf{g}_n | = | nominal geometry |
| l | = | number of outputs |
| m | = | number of inputs |
| n | = | number of states |
| n_r | = | number of reduced states |
| n_s | = | number of geometric mode shapes |
| t_f | = | final time |
| \mathbf{u} | = | input vector |
| v_i | = | geometric mode shape |
| \mathbf{x} | = | linearized state vector |

| | | |
|--------------------|---|--|
| \mathbf{x}_r | = | reduced state vector |
| \mathbf{x}_{ss} | = | steady-state solution |
| \mathbf{x}_0 | = | linearized state corresponding to the average geometry |
| \mathbf{x}^0 | = | initial condition |
| \mathbf{y} | = | output vector |
| \mathbf{y}_a | = | approximate output vector |
| \mathbf{y}_e | = | exact output vector |
| \mathbf{y}_o | = | nominal output vector |
| \mathbf{y}_r | = | reduced output vector |
| z_i | = | random numbers representing geometry variability |
| \mathbf{z}_{max} | = | upper bound of z |
| \mathbf{z}_{min} | = | lower bound of z |
| \mathbf{z}^* | = | optimal sample point |
| Δt | = | time step |
| ε | = | level of accuracy |
| σ_i | = | i th singular value of the geometry snapshot matrix |
| Φ | = | right reduced-basis matrix |
| Ψ | = | left reduced-basis matrix |
| \emptyset | = | the empty set |

I. Introduction

THE goal of model reduction is to systematically generate cost-efficient representations of large-scale systems that result, for example, from discretization of partial differential equations (PDEs). We present an approach for deriving reduced models for probabilistic analysis in large-scale unsteady aerodynamic applications. The key challenges that must be addressed in this setting are 1) the formulation of a computationally efficient representation of the parametric dependence that describes the uncertainty and 2) the derivation of reduced-order models that capture variation over a parametric input space.

Computational fluid dynamics (CFD) formulations lead to large-scale systems of equations that are computationally expensive to solve. In many unsteady aerodynamic applications, a small number of inputs and outputs of interest can be identified, and computationally efficient reduced-order models can be obtained that preserve the desired input–output mapping. For example, the proper orthogonal decomposition (POD) method of snapshots [1] has been used widely throughout CFD applications such as aeroelasticity [2–4] and flow control [5,6].

Presented as Paper 2049 at the 48th AIAA Structures, Structural Dynamics and Materials Conference, Waikiki, HI, 23–27 April 2007; received 25 November 2007; revision received 28 May 2008; accepted for publication 6 June 2008. Copyright © 2008 by T. Bui-Thanh, K. Willcox, and O. Ghattas. Published by the American Institute of Aeronautics and Astronautics, Inc., with permission. Copies of this paper may be made for personal or internal use, on condition that the copier pay the \$10.00 per-copy fee to the Copyright Clearance Center, Inc., 222 Rosewood Drive, Danvers, MA 01923; include the code 0001-1452/08 \$10.00 in correspondence with the CCC.

*Postdoctoral Associate, Department of Aeronautics and Astronautics; tanbui@mit.edu.

†Associate Professor, Department of Aeronautics and Astronautics; kwillcox@mit.edu. Senior Member AIAA.

‡Professor, Geological Sciences, Mechanical Engineering, Institute for Computational Engineering and Sciences; omar@ices.texas.edu.

Quantifying the impact of variations in input parameters on system outputs of interest is critical to a number of applications, such as shape design, probabilistic analyses, and structural analysis. For example, mistuning, or blade-to-blade variation, is an important consideration for aeroelastic analysis of bladed disks, because even small variations among blades can have a large impact on the forced response and, consequently, on the high-cycle fatigue properties of the engine. In such applications (in which the physical system must be simulated repeatedly for different inputs), the availability of reduced models can greatly facilitate the design and/or analysis task. However, to be useful in such a setting, the reduced model must provide an accurate representation of the high-fidelity CFD model over a wide range of parameters.

Most reduction techniques for large-scale systems employ a projection framework that uses a reduced-space basis. Methods to compute the basis in the large-scale setting include approximate balanced truncation [7–10], Krylov-subspace methods [11–13], POD [1, 14, 15], and reduced-basis methods [16, 17]. In the latter three cases, the quality of the reduced-order model is critically dependent on the information, generated from sampled solutions of the large-scale system, that is used to create the reduced basis. In general, selecting an appropriate set of samples to generate this information has been achieved in an ad hoc manner. Empirical knowledge of the problem at hand has been used to sample a parameter space to generate a POD or Krylov basis for cases in which the number of input parameters is small (for example, optimal control problems [5, 6, 18, 19] and parameterized design of interconnect circuits [20]) and for the case of multiple parameters describing inhomogeneous boundary conditions for time-dependent PDEs [21]. Extended reduced-order-modeling and spanning reduced-order-modeling methods have been developed to derive a basis that spans a parametric space and have been applied to uncertainty analysis of a structural problem [22].

For reduction of large-scale linear time-invariant systems using multipoint rational Krylov approximations, [23] proposes a systematic method for selecting interpolation points based on an optimality criterion. To address the more general challenge of sampling a high-dimensional parameter space to build a reduced basis, the greedy algorithm was introduced in [24–27]. The key premise of the greedy algorithm is to adaptively choose samples by finding the location of the maximum reduced-model error over a predetermined discrete set of parameters. The greedy algorithm was applied to find reduced models for the parameterized steady incompressible Navier–Stokes equations [25]. It was also combined with a posteriori error estimators for parameterized parabolic PDEs and was applied to several optimal control and inverse problems [26, 27].

Here, we formulate the task of determining appropriate sample locations as a greedy optimization problem, which is solved using an efficient adaptive algorithm. The optimization formulation treats the parameter space as continuous; that is, we do not require the a priori selection of a discrete parameter set. Further, our selection criterion uses an indicator of the error between full-order and reduced-order outputs; thus, our approach is applicable in cases for which error estimators are unavailable. Unlike other sampling methods, the optimization-based approach scales well to systems with a large number of parameters. To further address the challenge of achieving a computationally efficient representation of the dependence of the CFD model on geometric parameters, we propose a linearization strategy that yields an affine parametric dependence.

This article is organized as follows. Section II describes a parametrically affine model for capturing the effects of geometry variations on linearized unsteady aerodynamic response. Section III presents an overview of projection-based model reduction and then describes the proposed optimization-based approach used to determine the reduced basis. Section IV demonstrates the methodology through an example that considers the effects of variations in blade geometry on the forced response of a subsonic compressor blade row. Finally, Sec. V presents conclusions.

II. Linearized CFD Model with Geometric Variability

In this section, we briefly present the linearized CFD model that is used in this work. In many applications of interest, the unsteady flow solution can be assumed to be a small perturbation from steady-state conditions. This allows the unsteady governing equations to be linearized around the steady-state flow, which reduces the computational cost of solution considerably. Here, a discontinuous Galerkin finite element method is used (see [28, 29] for more details on the nonlinear steady-state model). Further, an approximation that employs an affine decomposition of the parametric dependence is used to incorporate geometric variability in a computationally efficient way.

The linearized equations can be written in standard state-space form:

$$\mathbf{E} \dot{\mathbf{x}} = \mathbf{A} \mathbf{x} + \mathbf{B} \mathbf{u} \quad (1)$$

$$\mathbf{y} = \mathbf{C} \mathbf{x} \quad (2)$$

where $\mathbf{x} \in \mathbb{R}^n$ is the state vector containing the n perturbations in flow unknowns from the steady-state solution \mathbf{x}_{ss} . The matrices $\mathbf{A} \in \mathbb{R}^{n \times n}$, $\mathbf{B} \in \mathbb{R}^{n \times m}$, $\mathbf{C} \in \mathbb{R}^{l \times n}$, and $\mathbf{E} \in \mathbb{R}^{n \times n}$ in Eqs. (1) and (2) have constant coefficients evaluated at steady-state conditions \mathbf{x}_{ss} and arise from the linearization of the nonlinear governing equations. The vector $\mathbf{u}(t) \in \mathbb{R}^m$ contains m external forcing inputs that are applied through boundary conditions such as the prescribed motion of the domain boundary or incoming flow disturbances. The vector $\mathbf{y}(t) \in \mathbb{R}^l$ contains l outputs of interest such as lift or moment coefficients.

We next consider incorporating the effects of geometry variability into the linearized unsteady CFD model. Following [30], a general geometry g can be expressed as

$$g = g_n + \bar{g} + \sum_{i=1}^{n_s} \sigma_i z_i v_i \quad (3)$$

where g_n is the nominal geometry, \bar{g} is the average geometric variation, v_i are geometric mode shapes, and n_s is the number of mode shapes used to represent the variation in geometry. The geometric mode shapes could be computed, for example, by performing principal component analysis (PCA) on a manufacturing sample of system geometries. In that case, the parameters z_i in Eq. (3) are random numbers distributed normally with zero mean and unit variance, $z_i \in N(0, 1)$, and σ_i is the i th singular value of the measurement snapshot matrix, which represents the geometric variability attributable to the i th mode; thus, the product $\sigma_i z_i$ is the amount by which the mode v_i contributes to the geometry g . A detailed description of the methodology underlying this geometric model can be found in [30].

Using model (3), a general geometry $g(\mathbf{z})$ is specified by the parameter vector $\mathbf{z} = [z_1, z_2, \dots, z_{n_s}]^T$, which describes the geometry variability in terms of the geometry modes. The linearized CFD system corresponding to geometry $g(\mathbf{z})$ is given by

$$\begin{aligned} \mathbf{E}(\mathbf{x}_{ss}(g(\mathbf{z})), g(\mathbf{z})) \dot{\mathbf{x}} \\ = \mathbf{A}(\mathbf{x}_{ss}(g(\mathbf{z})), g(\mathbf{z})) \mathbf{x} + \mathbf{B}(\mathbf{x}_{ss}(g(\mathbf{z})), g(\mathbf{z})) \mathbf{u} \end{aligned} \quad (4)$$

$$\mathbf{y} = \mathbf{C}(\mathbf{x}_{ss}(g(\mathbf{z})), g(\mathbf{z})) \mathbf{x} \quad (5)$$

where the CFD system matrices \mathbf{E} , \mathbf{A} , \mathbf{B} , and \mathbf{C} are, in general, both a nonlinear function of the geometry $g(\mathbf{z})$ and of the steady-state solution $\mathbf{x}_{ss}(g(\mathbf{z}))$, which is itself also a function of the geometry. To solve the CFD system (4) and (5) for each geometry g , we must do the following:

- 1) Compute the steady-state solution $\mathbf{x}_{ss}(g(\mathbf{z}))$.
- 2) Evaluate the linearized matrices \mathbf{E} , \mathbf{A} , \mathbf{B} , and \mathbf{C} .
- 3) Solve the resulting large-scale linear system.

This is a computationally prohibitive proposition for applications such as probabilistic analysis, in which thousands of geometry perturbations may be analyzed over many random samples of \mathbf{z} .

The expansion given by Eq. (3), which represents a general geometry as a perturbation about the average geometry, $g_0 = g_n + \bar{g}$, is used to derive an approximate model for representing the effects of geometry variations. For convenience of notation, we write the dependence of the CFD matrices on the parameter \mathbf{z} as $\mathbf{E}(\mathbf{x}_{ss}(g(\mathbf{z})), g(\mathbf{z})) = \mathbf{E}(\mathbf{z})$, $\mathbf{A}(\mathbf{x}_{ss}(g(\mathbf{z})), g(\mathbf{z})) = \mathbf{A}(\mathbf{z})$, $\mathbf{B}(\mathbf{x}_{ss}(g(\mathbf{z})), g(\mathbf{z})) = \mathbf{B}(\mathbf{z})$, and $\mathbf{C}(\mathbf{x}_{ss}(g(\mathbf{z})), g(\mathbf{z})) = \mathbf{C}(\mathbf{z})$. Instead of computing the linearized CFD matrices exactly for any \mathbf{z} , we choose to linearize the relationships $\mathbf{E}(\mathbf{z})$, $\mathbf{A}(\mathbf{z})$, $\mathbf{B}(\mathbf{z})$, and $\mathbf{C}(\mathbf{z})$. The linearized unsteady CFD model for the average geometry $g_0 = g_n + \bar{g}$ is defined by the matrices \mathbf{E}_0 , \mathbf{A}_0 , \mathbf{B}_0 , and \mathbf{C}_0 , with corresponding solution \mathbf{x}_0 . That is, for $\mathbf{z} = 0$, we have

$$\mathbf{E}_0 \dot{\mathbf{x}}_0 = \mathbf{A}_0 \mathbf{x}_0 + \mathbf{B}_0 \mathbf{u} \quad (6)$$

$$\mathbf{y}_0 = \mathbf{C}_0 \mathbf{x}_0 \quad (7)$$

Using a Taylor series expansion about $\mathbf{z} = 0$ for the matrix $\mathbf{A}(\mathbf{z})$ gives

$$\mathbf{A}(\mathbf{z}) = \mathbf{A}_0 + \left. \frac{d\mathbf{A}}{dz_1} \right|_{z=0} z_1 + \cdots + \left. \frac{d\mathbf{A}}{dz_{n_s}} \right|_{z=0} z_{n_s} + \cdots \quad (8)$$

where the matrix derivatives denote componentwise derivatives, which can be evaluated through application of the chain rule or numerically by finite differences. These derivatives are evaluated at average geometry conditions $\mathbf{z} = 0$, but reflect the dependence on \mathbf{z} in two ways: explicitly as well as implicitly through the dependence of \mathbf{x}_{ss} on \mathbf{z} . The matrices $\mathbf{E}(\mathbf{z})$, $\mathbf{B}(\mathbf{z})$, and $\mathbf{C}(\mathbf{z})$ can be expanded using formulas analogous to Eq. (8).

If the geometric variability (given by the product $\sigma_i z_i$) is sufficiently small, the constant and linear terms in the Taylor expansion (8) are sufficient to approximate the linearized matrices $\mathbf{A}(\mathbf{z})$ accurately: that is,

$$\mathbf{A}(\mathbf{z}) \approx \mathbf{A}_0 + \left. \frac{d\mathbf{A}}{dz_1} \right|_{z=0} z_1 + \cdots + \left. \frac{d\mathbf{A}}{dz_{n_s}} \right|_{z=0} z_{n_s} \quad (9)$$

For $i = 1, 2, \dots, n_s$, we define

$$\mathbf{E}'_i = \left. \frac{d\mathbf{E}}{dz_i} \right|_{z=0}, \quad \mathbf{A}'_i = \left. \frac{d\mathbf{A}}{dz_i} \right|_{z=0}, \quad \mathbf{B}'_i = \left. \frac{d\mathbf{B}}{dz_i} \right|_{z=0}, \quad \mathbf{C}'_i = \left. \frac{d\mathbf{C}}{dz_i} \right|_{z=0} \quad (10)$$

where the matrices \mathbf{E}'_i , \mathbf{A}'_i , \mathbf{B}'_i , and \mathbf{C}'_i can be computed, for example, using a finite difference approximation of the respective derivatives. The approximate CFD model for any \mathbf{z} is then given by

$$\underbrace{\left(\mathbf{E}_0 + \sum_{i=1}^{n_s} \mathbf{E}'_i z_i \right)}_{\mathbf{E}(\mathbf{z})} \dot{\mathbf{x}} = \underbrace{\left(\mathbf{A}_0 + \sum_{i=1}^{n_s} \mathbf{A}'_i z_i \right)}_{\mathbf{A}(\mathbf{z})} \mathbf{x} + \underbrace{\left(\mathbf{B}_0 + \sum_{i=1}^{n_s} \mathbf{B}'_i z_i \right)}_{\mathbf{B}(\mathbf{z})} \mathbf{u} \quad (11)$$

$$\mathbf{y} = \underbrace{\left(\mathbf{C}_0 + \sum_{i=1}^{n_s} \mathbf{C}'_i z_i \right)}_{\mathbf{C}(\mathbf{z})} \mathbf{x} \quad (12)$$

For simplicity, we approximate the matrix derivatives in Eqs. (11) and (12) using central differences. In this case, a total of

$$2 \sum_{i=1}^{n_s} + 1$$

large-scale steady-state CFD solves are required to determine the matrices \mathbf{A}_0 , \mathbf{B}_0 , \mathbf{C}_0 , \mathbf{E}_0 , \mathbf{A}'_i , \mathbf{B}'_i , \mathbf{C}'_i , and \mathbf{E}'_i . This is a one-time offline cost; once the matrices are computed, the system (11) and (12) can be readily evaluated for an arbitrary geometry $g(\mathbf{z})$ without running the CFD steady solver.

It should be noted that the model (11) and (12) is valid for only small variations from the average geometry and small unsteady perturbations from steady-state conditions. Larger geometric variations will incur larger errors in the solution of Eqs. (11) and (12), due to the neglect of the higher-order terms in the Taylor series expansion. Further, the forcing inputs $\mathbf{u}(t)$ must remain small in order for the state-linearization of the nonlinear CFD model to be valid. The specific range of acceptable input magnitudes will vary from problem to problem; however, linearized analysis has been shown to be appropriate in many application contexts, including aeroelasticity [3]. For example, Lisandrin et al. [31] show that for transonic flow over isolated airfoils analyzed with a nonlinear Euler model, unsteady pitching disturbances up to 500% in magnitude of the steady value can be considered linear with respect to perturbations of the displacements around the steady condition, as long as flow separations or shock/boundary-layer interactions do not occur. Even with the restriction of small geometric variations and small deviations from steady-state conditions, our model is useful for many practical applications.

Although these simplifications reduce the computational cost, the model (11) and (12) is still of high dimension and thus is computationally too expensive for applications such as probabilistic analysis, in which one needs to determine the unsteady aerodynamic response for many random geometries. In the next section, we propose a model-reduction method that enables us to further reduce the cost of solving the approximate CFD system. The key challenge that must be addressed is developing a reduced-order model that is accurate in both state space and geometric parameter space, described here by the vector \mathbf{z} .

III. Model-Reduction Methodology

A. General Projection Framework

Most large-scale model-reduction frameworks are based on a projection approach, which is described in general terms in this section. Consider the general parameterized dynamic system

$$\mathbf{E}(\mathbf{z}) \dot{\mathbf{x}} = \mathbf{A}(\mathbf{z}) \mathbf{x} + \mathbf{B}(\mathbf{z}) \mathbf{u} \quad (13)$$

$$\mathbf{y} = \mathbf{C}(\mathbf{z}) \mathbf{x} \quad (14)$$

with initial condition

$$\mathbf{x}(0) = \mathbf{x}^0 \quad (15)$$

where $\mathbf{x}(\mathbf{z}, t) \in \mathbb{R}^n$ is the state vector, $\mathbf{u}(t) \in \mathbb{R}^m$ contains the m forcing inputs to the system, $\mathbf{y}(\mathbf{z}, \mathbf{x}, t) \in \mathbb{R}^l$ contains the l outputs of interest, and \mathbf{x}^0 is the specified initial state. The matrices $\mathbf{E} \in \mathbb{R}^{n \times n}$, $\mathbf{A} \in \mathbb{R}^{n \times n}$, $\mathbf{B} \in \mathbb{R}^{n \times m}$, and $\mathbf{C} \in \mathbb{R}^{l \times n}$ in Eqs. (13) and (14) may depend (possibly nonlinearly) on a set of n_s parameters contained in the vector $\mathbf{z} \in \mathbb{R}^{n_s}$. General dynamic systems of the form in Eqs. (13–15) often arise from discretization of PDEs. In that case, the dimension of the system, n , is large, and the parameters z_i could describe, for example, changes in the domain shape or PDE coefficients. The CFD model (11) and (12) derived in the previous section is one example of a system of the form in Eqs. (13) and (14); in that case, the parameters z_i describe geometric shape variations.

A reduced-order model of Eqs. (13–15) can be derived by assuming that the state $\mathbf{x}(\mathbf{z}, t)$ is represented as a linear combination of n_r basis vectors:

$$\tilde{\mathbf{x}} = \Phi \mathbf{x}_r, \quad (16)$$

where $\tilde{\mathbf{x}}(\mathbf{z}, t)$ is the reduced-model approximation of the state $\mathbf{x}(\mathbf{z}, t)$ and $n_r \ll n$. The projection matrix $\Phi \in \mathbb{R}^{n \times n_r}$ contains as columns the basis vectors ϕ_i (i.e., $\Phi = [\phi_1 \phi_2 \cdots \phi_{n_r}]$), and the vector

$\mathbf{x}_r(\mathbf{z}, t) \in \mathbb{R}^{n_r}$ contains the corresponding modal amplitudes. Using the representation (16) together with a Petrov–Galerkin projection of the system (13–15) onto the space spanned by the left basis $\Psi \in \mathbb{R}^{n \times n_r}$, yields the reduced-order model with state $\mathbf{x}_r(\mathbf{z}, t)$ and output $\mathbf{y}_r(\mathbf{z}, \mathbf{x}, t)$:

$$\mathbf{E}_r(\mathbf{z})\dot{\mathbf{x}}_r = \mathbf{A}_r(\mathbf{z})\mathbf{x}_r + \mathbf{B}_r(\mathbf{z})\mathbf{u} \quad (17)$$

$$\mathbf{y}_r = \mathbf{C}_r(\mathbf{z})\mathbf{x}_r \quad (18)$$

$$\mathbf{x}_r^0 = \Psi^T \mathbf{x}(0) \quad (19)$$

where $\mathbf{E}_r(\mathbf{z}) = \Psi^T \mathbf{E}(\mathbf{z}) \Phi$, $\mathbf{A}_r(\mathbf{z}) = \Psi^T \mathbf{A}(\mathbf{z}) \Phi$, $\mathbf{B}_r(\mathbf{z}) = \Psi^T \mathbf{B}(\mathbf{z})$, and $\mathbf{C}_r(\mathbf{z}) = \mathbf{C}(\mathbf{z}) \Phi$.

Projection-based model-reduction techniques seek to find the bases Φ and Ψ such that the reduced system (17–19) provides an accurate representation of the large-scale system (13–15) over the desired range of inputs $\mathbf{u}(t)$ and parameters \mathbf{z} . A common choice for the left basis is the Galerkin projection $\Psi = \Phi$. In this work, we use a least-squares weighted-residual choice of the left basis, which amounts to $\Psi = (\mathbf{E} - \Delta t \mathbf{A}) \Phi$, where Δt is the time step used to discretize Eqs. (13) and (14). In many cases, a least-squares approach can be used to guarantee stability of the reduced model.

B. Reduced Basis for Parametric Input Dependence

Using the general projection framework, our model-reduction task becomes one of determining an appropriate reduced basis that spans both the parametric input space \mathbf{z} and the space of unsteady inputs $\mathbf{u}(t)$. In the case of a linear time- and parameter-invariant system [that is, a system of the form in Eqs. (13–15), with no dependence on parameters \mathbf{z}], a number of model-reduction techniques can be used, such as Krylov-based methods and POD. To extend these techniques to the general case in which the system matrices depend on the parameters \mathbf{z} , we require a systematic method of sampling the parametric input space.

In the case of the POD, the reduced basis is formed as the span of a set of state solutions, commonly referred to as snapshots. These snapshots are computed by solving the system (13–15) for selected values of the parameters \mathbf{z} and selected forcing inputs $\mathbf{u}(t)$. The quality of the resulting reduced-order model depends strongly on the choice of parameters and inputs over which snapshots are computed. Two issues arise in selecting an appropriate sample set. First, choosing where and how many samples to generate has been, in general, an ad hoc process. One can use knowledge of the application at hand to determine representative inputs; however, the resulting reduced-order model would not be of guaranteed quality. Second, in the case that the parametric input space is of high dimension, ad hoc generation of snapshots can require a prohibitive number of high-fidelity system solves. Using standard sampling methods, a problem with just a few parameters can require a large number of samples to adequately cover the space, due to the combinatorial explosion of the number of possible parameter combinations.

To address these issues, we use the greedy algorithm [24–27] to adaptively select snapshots, by finding the location in parameter space in which the error between the full-order and reduced-order models is maximal, updating the basis with information gathered from this sample location, forming a new reduced model, and repeating the process. In [32], a method is presented that formulates the greedy approach as an optimization problem that minimizes the error in reduced-model output prediction, which is defined by introducing (as constraints) the systems of equations representing the full and reduced models. In that work, the theoretical properties of the approach are described for steady problems. Here, we extend that approach to address unsteady problems, as described in the remainder of this section.

Within each cycle of the greedy algorithm, the key step is to determine the location in parameter space in which the error in the reduced model is maximal. We define the cost functional

$$\begin{aligned} \mathcal{G}(\mathbf{z}, \mathbf{x}, \mathbf{x}_r) &= \frac{1}{2} \int_0^{t_f} \|\mathbf{y}(\mathbf{z}, \mathbf{x}, t) - \mathbf{y}_r(\mathbf{z}, \mathbf{x}_r, t)\|_2^2 dt \\ &= \frac{1}{2} \int_0^{t_f} \|\mathbf{C}\mathbf{x} - \mathbf{C}_r\mathbf{x}_r\|_2^2 dt \end{aligned} \quad (20)$$

which describes the error between the full and reduced models over the parameter space \mathbf{z} , integrated over some time horizon of interest t_f . Given a current basis Φ , we find the location in parameter space of maximum error by solving the optimization problem

$$\max_{\mathbf{x}, \mathbf{x}_r, \mathbf{z}} \mathcal{G} = \frac{1}{2} \int_0^{t_f} \|\mathbf{C}\mathbf{x} - \mathbf{C}_r\mathbf{x}_r\|_2^2 dt \quad (21)$$

subject to

$$\mathbf{E}(\mathbf{z})\dot{\mathbf{x}} = \mathbf{A}(\mathbf{z})\mathbf{x} + \mathbf{B}(\mathbf{z})\mathbf{u} \quad (22)$$

$$\mathbf{x}^0 = \mathbf{x}(0) \quad (23)$$

$$\mathbf{E}_r(\mathbf{z})\dot{\mathbf{x}}_r = \mathbf{A}_r(\mathbf{z})\mathbf{x}_r + \mathbf{B}_r(\mathbf{z})\mathbf{u} \quad (24)$$

$$\mathbf{x}_r^0 = \Phi^T \mathbf{x}(0) \quad (25)$$

$$\mathbf{z}_{\min} \leq \mathbf{z} \leq \mathbf{z}_{\max} \quad (26)$$

where \mathbf{z}_{\min} and \mathbf{z}_{\max} are, respectively, lower and upper bounds on the parameter vector \mathbf{z} . We denote the parameter vector that solves the maximization problem (21–26) by \mathbf{z}^* . Next, we compute the solution $\mathbf{x}(\mathbf{z}^*, t)$ of the full system at the worst-case parameter value \mathbf{z}^* . This solution information is added to the basis Φ , for example, using the POD. (Note that once the sample location has been found, other model-reduction methods could also be employed.) The procedure is then repeated by solving the optimization problem (21–26) with the updated basis Φ . Thus, we are using a systematic adaptive error metric based on the ability of the reduced-order model to capture the outputs of interest in order to choose the sample locations. This model-reduction approach is summarized in the following model-constrained adaptive sampling procedure.

Algorithm 1:

- 1) Given a reduced basis Φ , solve the optimization problem (21–26) to find the location in parameter space at which the error is maximized [i.e., find $\mathbf{z}^* = \arg \max \mathcal{G}(\mathbf{z})$].
- 2) If $\mathcal{G}(\mathbf{z}^*) < \varepsilon$, where ε is the desired level of accuracy, then terminate the algorithm. If not, go to the next step.
- 3) With $\mathbf{z} = \mathbf{z}^*$, solve the full system (13–15) to compute the state solutions $\mathbf{x}(\mathbf{z}^*, t)$, $t = (0, t_f)$. Use the span of these state solutions to update the basis Φ . Go to step 1.

In step 3 of Algorithm 1, the basis can be updated using many of the existing model-reduction methods. For example, the POD could be used to compute the span of the updated snapshot set, which would comprise the existing basis vectors and the new state solutions $\mathbf{x}(\mathbf{z}^*, t)$. As an alternative approach, one could also solve an (inner) optimization problem to find the basis that minimizes the output error at the sample points [33]. Algorithm 1 is initialized by choosing the initial basis as the empty set, $\Phi = \emptyset$; thus, the reduced model is initially a zero-order approximation of the full model.

The optimization problem (21–26) that must be solved in each adaptive cycle (i.e., step 1 of Algorithm 1) is large-scale; in particular, note that the large-scale system equations appear as constraints in Eq. (22). The determination of each sample point \mathbf{z}^* via solution of this optimization problem therefore requires some number of solves of the system (22), which, for the large-scale problems of interest here ($n > 10^5$), is the dominant computational cost. It is therefore critical to use an efficient optimization method: that is, one that exploits the structure of the problem to offer rapid

convergence to the optimum with the fewest number of full-model solves. We employ recent advances in scalable algorithms for large-scale optimization of systems governed by PDEs, which have permitted solution of problems with millions of state and optimization variables, often at a cost of a handful of PDE solves [34]. Our solution method is described in detail in [32]; in the following, we summarize the approach.

To solve the constrained optimization problem (21–26), we choose to solve an equivalent bound-constrained optimization problem in the \mathbf{z} variables by eliminating the state variables \mathbf{x} and \mathbf{x}_r . That is, we replace $\min_{\mathbf{x}, \mathbf{x}_r, \mathbf{z}} \mathcal{G}(\mathbf{x}, \mathbf{x}_r, \mathbf{z})$ with $\min_{\mathbf{z}} \mathcal{G}(\mathbf{x}(\mathbf{z}), \mathbf{x}_r(\mathbf{z}), \mathbf{z})$, where the dependence of \mathbf{x} and \mathbf{x}_r on \mathbf{z} is implicit through the full and reduced state equations (22–25). To handle the bound constraints, we use the Coleman–Li subspace trust-region interior-reflective Newton framework to solve the resulting bound-constrained optimization problem efficiently [35]. We use the conjugate gradient (CG) method to determine the subspace over which the linear system of equations arising at each Newton step is solved, and we globalize via a trust-region scheme (see, for example, [36]). This method combines the rapid locally quadratic convergence-rate properties of Newton’s method, the effectiveness of trust-region globalization for treating ill-conditioned problems, and the Eisenstat–Walker idea of preventing oversolving [37].

The gradient of \mathcal{G} with respect to \mathbf{z} , as required by Newton’s method, can be computed efficiently via an adjoint formulation, which, in this context, entails a pair of full and reduced state-system solves followed by a pair of full and reduced adjoint-system solves. CG requires only Hessian vector products and not the Hessian by itself; because it is a directional derivative of the gradient, its computation similarly involves solution of (linearized) state and adjoint equations. In summary, the work at each CG iteration of the optimization algorithm is dominated by the solution of a pair of state and adjoint systems.

As an alternative to using the true error function in Eq. (21), one can use an error indicator based on the residual of the full model evaluated at $\tilde{\mathbf{x}}$, the reduced-model approximation of the state. In this case, the optimization problem becomes

$$\max_{\mathbf{x}, \mathbf{z}} \mathcal{G} = \frac{1}{2} \int_0^{t_f} \|\mathbf{E} \Phi \dot{\mathbf{x}}_r - \mathbf{A} \Phi \mathbf{x}_r - \mathbf{B} \mathbf{u}\|_2^2 dt \quad (27)$$

subject to

$$\mathbf{E}_r(\mathbf{z}) \dot{\mathbf{x}}_r = \mathbf{A}_r(\mathbf{z}) \mathbf{x}_r + \mathbf{B}_r(\mathbf{z}) \mathbf{u} \quad (28)$$

$$\mathbf{x}_r^0 = \Phi^T \mathbf{x}(0) \quad (29)$$

$$\mathbf{z}_{\min} \leq \mathbf{z} \leq \mathbf{z}_{\max} \quad (30)$$

The advantage of this formulation is that the full-model equations no longer appear as constraints. Therefore, solution of the full model is avoided during the optimization solution (that is, in step 1 of Algorithm 1) and required only to generate the snapshots at the sample point in step 3. When high offline costs can be tolerated, using the true error is expected to lead to the identification of better sample points; however, when offline costs are a concern, the error indicator provides an attractive lower-cost option.

Regardless of the form of the objective function, the states depend nonlinearly on the parameter \mathbf{z} . Therefore, the optimization problems (21–26), which involve both full and reduced states, and Eqs. (27–30), which involve the reduced state, are generally nonconvex. In particular, as the model-constrained adaptive sampling procedure adds sample points, we expect the cost functional to become increasingly multimodal, because the error function will be close to zero (below the tolerance ε) at each of the previous parameter sample locations. Note that although finding the global maximum is preferred, convergence to a local maximum is still very useful; solving the greedy optimization problem is a

heuristic to systematically find good sample points, and at a local maximum, the error is (locally) large. To avoid convergence to a local maximum close to a previous sample location, and thus to explore the parameter space more widely, a random initialization of the optimization variables \mathbf{z} is used for each cycle of Algorithm 1. An initial guess is accepted only if it is sufficiently far from previous sample locations, measured using a tolerance that is set relative to the parameter ranges. The stopping criterion applied in step 2 of Algorithm 1 monitors $\mathcal{G}(\mathbf{z}^*)$, the reduced-model error associated with the optimal solution \mathbf{z}^* . It is important to note that if $\mathcal{G}(\mathbf{z}^*)$ falls below the desired error level, this guarantees only that the local error between the full and reduced model is sufficiently small. Because of the nonconvexity of the optimization problem, it is possible that larger errors may exist elsewhere in the parameter space. This also implies that the maximum error or residual $\mathcal{G}(\mathbf{z}^*)$ could increase in the next adaptive cycle.

C. Reduced-Order Linearized Aerodynamic Model with Geometric Variability

Combining the linearized unsteady model with geometric variability from Sec. II with the reduced-basis model-reduction methodology based on model-constrained adaptive sampling, we now have a method to create efficient reduced-order models that capture the effects of small geometric variations.

Using the projection framework and a basis Φ computed using Algorithm 1, the reduced-order model of Eqs. (11) and (12) is

$$\underbrace{\left(\mathbf{E}_{r_0} + \sum_{i=1}^{n_s} \mathbf{E}'_{r_i} z_i \right)}_{\mathbf{E}_r(\mathbf{z})} \dot{\mathbf{x}}_r = \underbrace{\left(\mathbf{A}_{r_0} + \sum_{i=1}^{n_s} \mathbf{A}'_{r_i} z_i \right)}_{\mathbf{A}_r(\mathbf{z})} \mathbf{x}_r + \underbrace{\left(\mathbf{B}_{r_0} + \sum_{i=1}^{n_s} \mathbf{B}'_{r_i} z_i \right)}_{\mathbf{B}_r(\mathbf{z})} \mathbf{u} \quad (31)$$

$$\mathbf{y}_r = \underbrace{\left(\mathbf{C}_{r_0} + \sum_{i=1}^{n_s} \mathbf{C}'_{r_i} z_i \right)}_{\mathbf{C}_r(\mathbf{z})} \mathbf{x}_r \quad (32)$$

where the reduced-order matrices are given by

$$\mathbf{E}_{r_0} = \Psi^T \mathbf{E}_0 \Phi, \quad \mathbf{A}_{r_0} = \Psi^T \mathbf{A}_0 \Phi, \quad \mathbf{B}_{r_0} = \Psi^T \mathbf{B}_0, \quad \mathbf{C}_{r_0} = \mathbf{C}_0 \Phi \quad (33)$$

$$\mathbf{E}'_{r_i} = \Psi^T \mathbf{E}'_i \Phi, \quad \mathbf{A}'_{r_i} = \Psi^T \mathbf{A}'_i \Phi, \quad \mathbf{B}'_{r_i} = \Psi^T \mathbf{B}'_i \quad (34)$$

$$\mathbf{C}'_{r_i} = \mathbf{C}'_i \Phi, \quad i = 1, 2, \dots, n_s$$

The key enabling feature of the adaptive sampling approach is that it allows the basis Φ to be computed in an efficient systematic manner, even when the dimension of the parameter space is large. The methodology also gives us a means to monitor the (local) error between reduced-order and full-order outputs. The key advantage of the geometric variability model is that it leads to an affine parameter dependence; thus, the reduced-order matrices in Eqs. (33) and (34) can be evaluated offline, and the online cost of solving the reduced-order model (31) and (32), does not depend on the large-scale state dimension n .

IV. Probabilistic Analysis Application

The model-reduction methodology is applied to probabilistic analysis of a subsonic rotor blade that moves in unsteady rigid motion. The analysis seeks to quantify the effects on the blade forced response of small variations in blade geometry. Mistuning, or blade-to-blade variation, is an important consideration for aeroelastic analysis of bladed disks, because even small variations among blades can have a large impact on the forced response and, consequently, on the high-cycle fatigue properties of the engine. The effects of blade structural mistuning (variations in mass and stiffness properties) have been studied extensively (see, for example, [38–41]); however,

due to the prohibitively high computational cost of performing probabilistic analysis with a CFD model, the aerodynamic effects due to variations in geometry are less understood.

Geometric mistuning effects have been incorporated into structural responses of bladed disks using a mode-acceleration method to convert the effect of geometric mistuning to that of external forces of the tuned disks [42]. Truncated sets of tuned system modes compensated by static modes (generated by external forces that were constructed from mistuning) were then used to obtain efficient and accurate structural reduced models. Several studies have also found that a small number of PCA geometric modes can capture manufactured variability in bladed disks accurately [30,43,44]. Such reduced geometric variability models have been used to investigate the impact of geometric variability on axial compressor steady aerodynamic performance using Monte Carlo simulation (MCS) based on a large-scale nonlinear CFD model [30]. Using MCS of a CFD model to quantify the impact of geometric variability on *unsteady* performance is a computationally prohibitive proposition. For example, if the unsteady analysis for one geometry takes 1 min to compute (a conservative estimate), the $\mathcal{O}(50,000)$ such analyses that would be required for a MCS would take roughly one month of CPU time. Therefore, we desire to obtain a reduced-order model that captures both unsteady response and variation over blade geometries. Our method combines the reduced geometric variability model and the model-constrained adaptive sampling methodology of Algorithm 1 to obtain a reduced-order model that is valid over a range of forcing frequencies, aerodynamic damping, and small perturbations in blade geometries and thus enables fast and accurate probabilistic analysis.

A. Blade Forced-Response Example

For the example presented here, the flow is modeled using the two-dimensional Euler equations written at the blade midsection. The average geometry of the blade is shown in Fig. 1, along with the unstructured grid for a single blade passage, which contains 4292 triangular elements. The Euler equations are discretized in space with the discontinuous Galerkin method described in Sec. II. For the case considered here, the incoming steady-state flow has a Mach number of $M = 0.113$ and a flow angle of $\beta = 59$ deg. Flow tangency boundary conditions are applied on the blade surfaces. To compute the steady-state flow for the nominal case, we exploit the fact that the rotor is cyclically symmetric; thus, the steady flow in each blade passage is the same and the steady-state solution can be computed on a computational domain that describes just a single blade passage. Periodic boundary conditions are applied on the upper and lower boundaries of the grid to represent the effects of neighboring blade passages.

A linearized model is derived for unsteady flow computations by assuming that the unsteady flow is a small deviation from steady

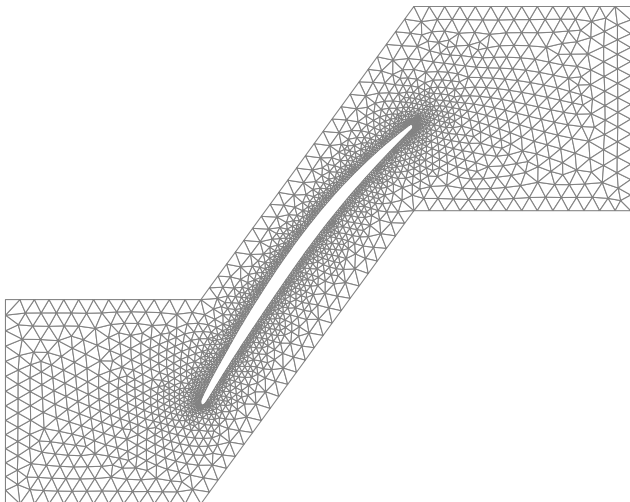


Fig. 1 Geometry and CFD mesh for a single blade passage.

state. An affine dependence of the linearized system matrices on the blade geometries is derived using the method described in Sec. II. This leads to a system of the form in Eqs. (11) and (12), in which the state vector $\mathbf{x}(t)$ contains the unknown perturbation flow quantities (density, Cartesian momentum components, and energy). For the discontinuous Galerkin formulation, the states are the coefficients corresponding to each nodal finite element shape function. Using linear elements, there are 12 degrees of freedom per element, giving a total state-space size of $n = 51$, 504 states per blade passage. For the problem considered here, the forcing input $\mathbf{u}(t)$ describes the unsteady motion of each blade, which, in this case, is assumed to be rigid plunging motion (vertical motion with no rotation). The outputs of interest $\mathbf{y}(t)$ are the unsteady lift forces generated on each blade. The initial perturbation flow is given by $\mathbf{x}^0 = 0$.

B. Geometric Variability Model

Geometric modes were computed using a PCA of data modified from 145 actual blades, measured at 13 sections along the radial direction. The midsection geometries were then extracted. Thus, the parameter vector \mathbf{z} contains the normally distributed random variables that describe perturbations in the geometry of each blade according to the model (3). The first five z_i coefficients were computed for each of the 145 blade geometries. The Kolmogorov–Smirnov test indicates that we cannot reject the null hypothesis that these coefficients were drawn from a standard normal distribution. In Fig. 2, we consider a geometric model that uses the two dominant variability modes (i.e., the modes corresponding to the two largest singular values), $n_s = 2$. The figure shows the lift coefficient C_L and moment coefficient C_M of a blade in response to a pulse input in plunge for a particular geometry that corresponds to $z_1 = 1.59$ and $z_2 = 1.59$. The response is computed using the exact linearized CFD model [i.e., the system (4) and (5)] and the approximate CFD model (11) and (12) with $n_s = 2$ geometry modes]. For reference, the response of the nominal blade is also shown in the figure. It can be seen that despite the small perturbation in geometry, the change in lift- and moment-coefficient responses is significant. The approximate CFD model captures the unsteady response accurately.

Table 1 shows the error in lift and moment outputs due to the linearized geometry approximation for several different blade geometries with a pulse input in plunge. The error e is defined as the 2-norm of the difference between the approximate, and the exact linearized CFD output is defined as a percentage of the change between the exact and the nominal output:

$$e = \frac{\sqrt{\int_0^{t_f} \|\mathbf{y}_e - \mathbf{y}_a\|_2^2 dt}}{\sqrt{\int_0^{t_f} \|\mathbf{y}_e - \mathbf{y}_o\|_2^2 dt}} \times 100\% \quad (9)$$

where \mathbf{y}_e , \mathbf{y}_a , and \mathbf{y}_o are, respectively, the exact, approximate, and nominal outputs. In Table 1, e_{C_M} denotes the error in moment-coefficient response, and e_{C_L} denotes the error in lift-coefficient response. These computations were carried out over the time horizon shown in Fig. 2 (i.e., with $t_f = 107$). In general, we expect the quality of the approximate model to be compromised as the size of the geometric perturbation increases. The errors shown in Table 1 for blade geometries in the tails of the distribution (i.e., those with large geometry variation) are deemed to be acceptable for the probabilistic application of interest here. For applications in which greater accuracy for large geometry variations is important (for example, determining the probability of failure would require the tail of the distribution to be resolved accurately), the results suggest that the approximate CFD system is not appropriate. In such cases, one might consider including more terms in Eq. (9), the Taylor series expansion of the CFD matrices.

C. Model Reduction

To create a reduced-order model for use in probabilistic analysis, the model-constrained adaptive sampling methodology of Algorithm 1 is applied to this problem. Results are shown here for the case of two blades moving with an interblade phase angle of

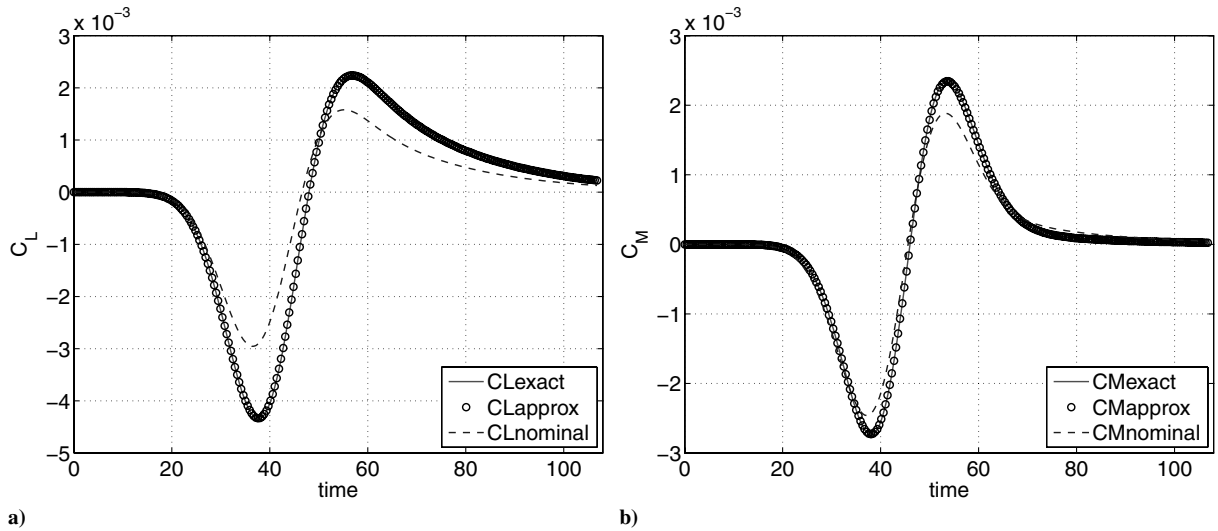


Fig. 2 Lift coefficient C_L and moment coefficient C_M in response to a pulse input in blade plunge displacement for the nominal geometry and a perturbed geometry described by two geometric PCA modes with $z_1 = 1.59$, $z_2 = 1.59$. Perturbed geometry results are computed with both the exact and approximate linearized CFD model.

180 deg. Each blade geometry is represented by five variability modes, giving $n_s = 10$ geometric parameters in this example. The geometric variability parameters \mathbf{z} , by construction, are random numbers normally distributed with zero mean and unity variance, 99.7% of which are distributed in the interval $[-3.0, 3.0]$. The bound constraints for all parameters in the greedy optimization problem are therefore chosen to be

$$-3.0 \leq z_i \leq 3.0, \quad i = 1, \dots, n_s \quad (36)$$

The model-constrained adaptive sampling methodology is employed using the residual error indicator given in Eq. (27). With a stopping tolerance of $\varepsilon = 10^{-4}$ and with the lift coefficients as the outputs of interest, this leads to a reduced-order model of size $n_r = 290$ (for two blades). Algorithm 1 required 29 adaptive cycles. Because the greedy optimization formulation (27–30) in this case does not involve the full model as constraints, the computational cost to compute our reduced model was thus of the order of 29 full-scale matrix factorizations (for which the computational cost dominates the other calculations). In terms of CPU time, this corresponds to 10.92 h on a dual-core 64-bit personal computer with a 3.2-GHz Pentium processor. Figure 3 shows the norm of the maximum residual versus the number of adaptive cycles. The overall trend is a decrease in residual norm, although the decrease is not monotonic. This is because our local optimization solver is only guaranteed to converge to a local maximum, the location of which depends on the initial guess supplied in each adaptive cycle. As a result, the current local maximizer may lead to a residual that has a larger norm than that of a maximizer on an earlier cycle. Although finding the global maximum is obviously preferable, a local maximum still provides us with a good sample point (the error is locally large for this geometry), and as the figure shows, after 20 adaptive cycles, the norm of the residual for all sampled points is small.

Table 1 Error in approximate CFD model predictions for a pulse input in blade displacement for several different geometries

| Variability amplitudes | $e_{C_M}, \%$ | $e_{C_L}, \%$ |
|----------------------------|---------------|---------------|
| $z_1 = 1.59, z_2 = 1.59$ | 5.04 | 2.6 |
| $z_1 = 1.59, z_2 = -1.59$ | 0.3 | 0.1 |
| $z_1 = -1.59, z_2 = -1.59$ | 2.0 | 0.8 |
| $z_1 = 3.0, z_2 = 3.0$ | 16.6 | 9.2 |
| $z_1 = 3.0, z_2 = -3.0$ | 4.1 | 2.3 |
| $z_1 = -3.0, z_2 = -3.0$ | 12.4 | 4.7 |

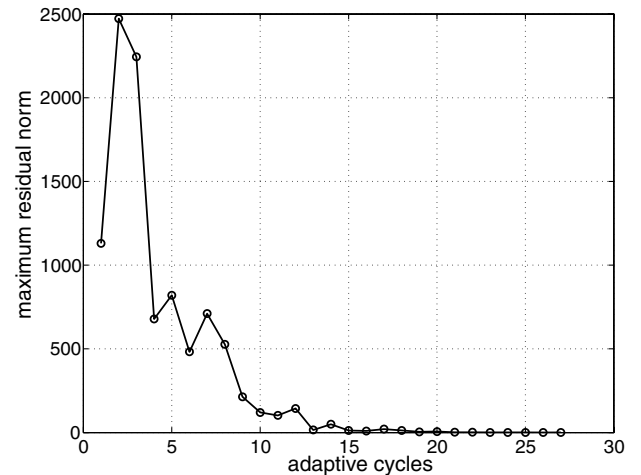


Fig. 3 Maximum residual norm versus the number of adaptive cycles.

We now have a reduced model of size $n_r = 290$ that accurately captures the unsteady response of the original two-blade system with $n = 103,008$ states over the range of geometries described by the 10 geometric parameters. As an example of an application for which this reduced model is useful, we consider probabilistic analysis of the system. Specifically, we consider the impact of blade geometry variabilities on the work per cycle, which is defined as the integral of the blade motion times the lift force over one unsteady cycle. A MCS was performed in which 10,000 blade geometries were selected randomly from the given distributions for each blade. The same 10,000 geometries were analyzed using the approximate CFD model and the reduced model. Figure 4 shows the resulting probability density functions (PDFs) of work per cycle for the first blade, computed using the approximate CFD model and the reduced-order model. Figure 5 shows the PDFs of work per cycle for the second blade. Table 2 shows that the CPU time required to compute the reduced model MCS is a factor of 468 times smaller than that required for the CFD MCS and more than justifies the offline cost required to compute the reduced model. These computational results were obtained on a dual-core 64-bit personal computer with a 3.2-GHz Pentium processor, using a direct sparse solver for the full model [45] and an LU decomposition for the reduced model.

Table 2 also compares the statistics of the two distributions. It can be seen from Figs. 4 and 5 and Table 2 that the reduced-order model accurately predicts the mean, variance, and shape of the distribution

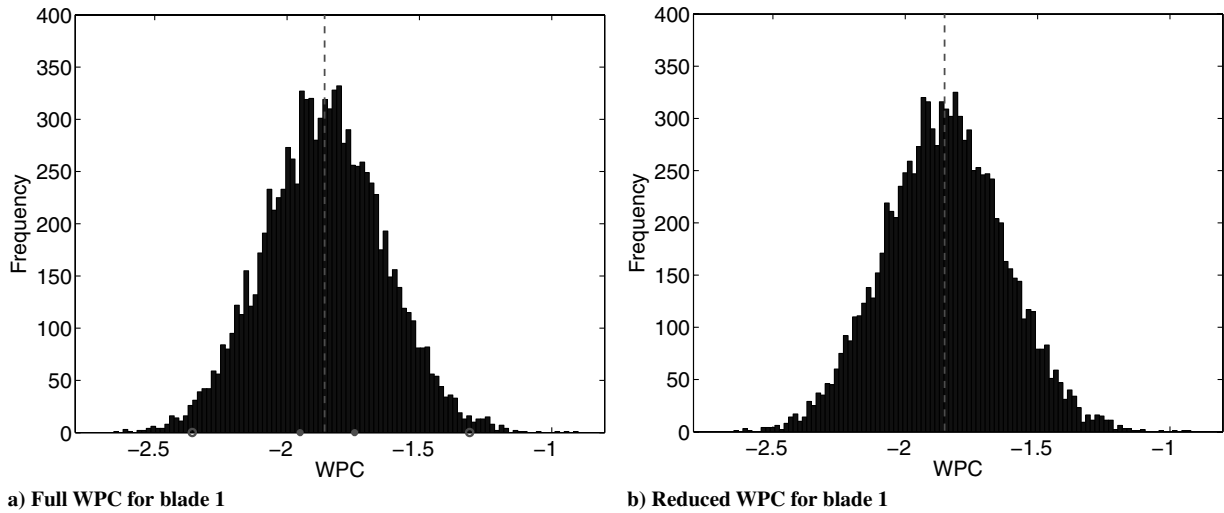


Fig. 4 Comparison of CFD and reduced-order-model predictions of work per cycle (WPC) for blade 1. MCS results are shown for 10,000 blade geometries. The same geometries were analyzed in each case. The dashed line denotes the mean.

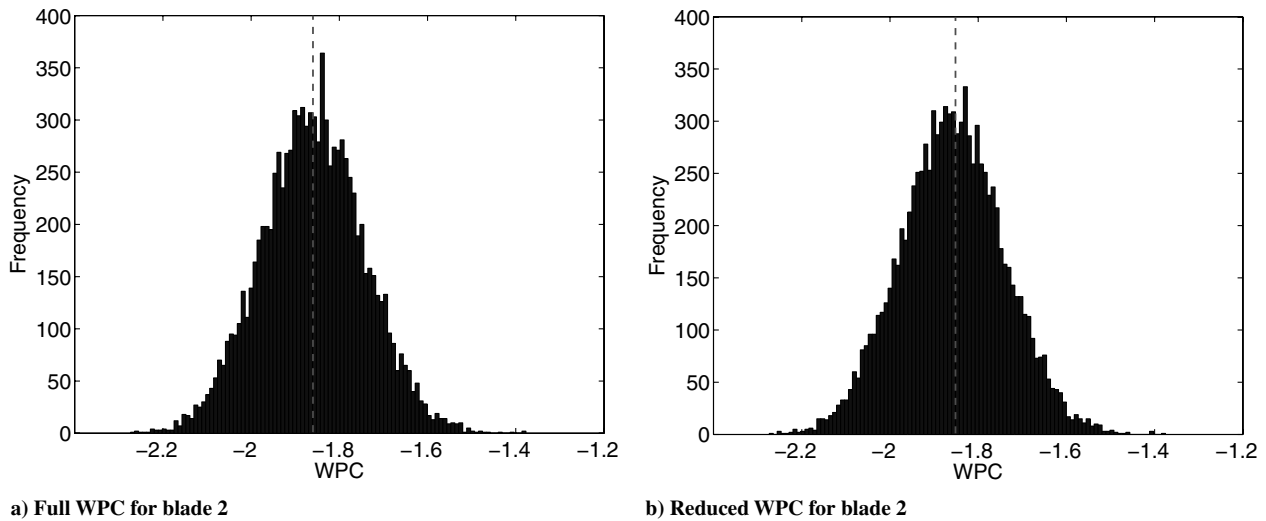


Fig. 5 Comparison of CFD and reduced-order-model predictions of work per cycle (WPC) for blade 2. MCS results are shown for 10,000 blade geometries. The same geometries were analyzed in each case. The dashed line denotes the mean.

of work per cycle. To further verify the quality of the reduced model, we apply the Kolmogorov–Smirnov method [46] to test whether the reduced work-per-cycle results and the full work-per-cycle results are drawn from the same distribution. The results show that we cannot reject the hypothesis that the distribution is the same at a 5% significance level.

To further compare the reduced-order and CFD results, we pick four particular geometries corresponding to the left tail, right tail,

midleft and midright locations on the PDF of the first blade, as indicated by the circles in Fig. 4a. In Table 3, the work per cycle is given for these four blade geometries as computed by the exact linearized CFD model, the approximate CFD model, and the reduced-order model. The table shows that the approximate CFD is again in acceptable agreement with the exact CFD for the midleft and midright cases, which have smaller variability. The errors in the tails of the distribution are larger. The effectiveness of the adaptive model-reduction methodology of Algorithm 1 can be seen from the good agreement between the approximate CFD and the reduced-model results for all four geometries.

Table 2 Approximate linearized CFD model and reduced-order-model MCS results. Work per cycle (WPC) is predicted for blade plunging motion at an interblade phase angle of 180 deg for 10,000 randomly selected blade geometries

| | Approximate linearized CFD | Reduced |
|----------------------|----------------------------|---------|
| Model size | 103,008 | 290 |
| Number of nonzeros | 2,846,056 | 84,100 |
| Offline cost | — | 10.92 h |
| Online cost | 515.61 h | 1.10 h |
| Blade 1 WPC mean | -1.8583 | -1.8515 |
| Blade 1 WPC variance | 0.0503 | 0.0506 |
| Blade 2 WPC mean | -1.8599 | -1.8583 |
| Blade 2 WPC variance | 0.0136 | 0.0138 |

Table 3 Linearized CFD, approximate linearized CFD, and reduced-order-model work-per-cycle prediction for the four geometries indicated in Fig. 4a

| | Linearized CFD | Approximate linearized CFD | Reduced |
|------------|----------------|----------------------------|---------|
| Left tail | -1.9576 | -2.3581 | -2.3585 |
| Midleft | -1.9099 | -1.9509 | -1.9341 |
| Midright | -1.8577 | -1.7448 | -1.7317 |
| Right tail | -1.9206 | -1.3098 | -1.3025 |

V. Conclusions

The key contributions of this paper are the derivation of a linearized CFD model that permits the effects of geometry variations to be represented with an explicit affine function, the development of an adaptive sampling method to derive a reduced-order basis that spans both unsteady forcing input and parameter space, and the solution of a large-scale probabilistic analysis of the effects of small variations in geometry on unsteady aerodynamic response. The methodology was demonstrated here for a problem that is linear in the state variables and affine in the parameter variables; however, the model-constrained adaptive sampling approach provides a general framework that is applicable to nonlinear problems. In the general nonlinear case, however, one must address the challenge of carrying out online reduced-order-model computations in an efficient manner that does not depend on the large-scale system dimension.

A Lagrange basis has been used in this work; however, one could further enrich the reduced subspace using a Hermite basis. Namely, one could add the derivatives of the states with respect to parameters as additional snapshots if they are easy and inexpensive to compute. An alternative approach might be to add the adjoint information to enrich the reduced basis. These approaches would likely reduce the offline cost of the algorithm by providing additional information at each sample point; however, a key question is whether the quality of the reduced model would be improved for a given basis size. These avenues provide interesting avenues for further research.

Acknowledgments

This work was partially supported by the Computational Engineering Program of the Singapore and Massachusetts Institute of Technology Alliance of the Universal Technology Corporation under contract number 04-S530-0022-07-C1, technical contract monitor C. Cross of the U.S. Air Force Research Laboratory, the U.S. Air Force Office of Scientific Research under grant number FA9550-06-0271, program manager Fariba Fahroo, and the National Science Foundation under Dynamic Data Driven Applications Systems (DDDAS) grants CNS-0540372 and CNS-0540186, program director Frederica Darema.

References

- [1] Sirovich, L., "Turbulence and the Dynamics of Coherent Structures, Part 1: Coherent Structures," *Quarterly of Applied Mathematics*, Vol. 45, No. 3, Oct. 1987, pp. 561–571.
- [2] Romanowski, M., "Reduced Order Unsteady Aerodynamic and Aeroelastic Models Using Karhunen-Loève Eigenmodes," AIAA Paper 96-194, 1996.
- [3] Dowell, E., and Hall, K., "Modeling of Fluid-Structure Interaction," *Annual Review of Fluid Mechanics*, Vol. 33, 2001, pp. 445–490. doi:10.1146/annurev.fluid.33.1.445
- [4] Lieu, T., Farhat, C., and Lesoinne, M., "Reduced-Order Fluid/Structure Modeling of a Complete Aircraft Configuration," *Computer Methods in Applied Mechanics and Engineering*, Vol. 195, Nos. 41–43, 2006, pp. 5730–5742. doi:10.1016/j.cma.2005.08.026
- [5] Hinze, M., and Volkwein, S., "Proper Orthogonal Decomposition Surrogate Models for Nonlinear Dynamical Systems: Error Estimates and Suboptimal Control," *Dimension Reduction of Large-Scale Systems*, edited by P. Benner, V. Mehrmann, and D. Sorensen, Lecture Notes in Computational Science and Engineering, Springer, New York, 2005, pp. 261–306.
- [6] Kunisch, K., and Volkwein, S., "Control of Burgers' Equation by Reduced Order Approach Using Proper Orthogonal Decomposition," *Journal of Optimization Theory and Applications*, Vol. 102, No. 2, 1999, pp. 345–371. doi:10.1023/A:1021732508059
- [7] Gugercin, S., and Antoulas, A., "A Survey of Model Reduction by Balanced Truncation and Some New Results," *International Journal of Control*, Vol. 77, No. 8, 2004, pp. 748–766. doi:10.1080/00207170410001713448
- [8] Li, J., and White, J., "Low Rank Solution of Lyapunov Equations," *SIAM Journal on Matrix Analysis and Applications*, Vol. 24, No. 1, 2002, pp. 260–280. doi:10.1137/S0895479801384937
- [9] Penzl, T., "Algorithms for Model Reduction of Large Dynamical Systems," *Linear Algebra and Its Applications*, Vol. 415, No. 2–3, June 2006, pp. 322–343. doi:10.1016/j.laa.2006.01.007
- [10] Sorensen, D., and Antoulas, A., "The Sylvester Equation and Approximate Balanced Reduction," *Linear Algebra and Its Applications*, Vol. 351–352, Aug. 2002, pp. 671–700. doi:10.1016/S0024-3795(02)00283-5
- [11] Feldmann, P., and Freund, R., "Efficient Linear Circuit Analysis by Padé Approximation via the Lanczos Process," *IEEE Transactions on Computer-Aided Design of Integrated Circuits and Systems*, Vol. 14, No. 5, 1995, pp. 639–649. doi:10.1109/43.384428
- [12] Gallivan, K., Grimme, E., and Van Dooren, P., "Padé Approximation of Large-Scale Dynamic Systems with Lanczos Methods," *Proceedings of the 33rd IEEE Conference on Decision and Control*, Inst. of Electrical and Electronics Engineers, Piscataway, NJ, Dec. 1994, pp. 443–448.
- [13] Grimme, E., "Krylov Projection Methods for Model Reduction," Ph.D. Thesis, Coordinated-Science Lab. Univ. of Illinois at Urbana-Champaign, Urbana-Champaign, IL, 1997.
- [14] Deane, A., Kevrekidis, I., Karniadakis, G., and Orszag, S., "Low-Dimensional Models for Complex Geometry Flows: Application to Grooved Channels and Circular Cylinders," *Physics of Fluids A*, Vol. 3, No. 10, 1991, pp. 2337–2354. doi:10.1063/1.857881
- [15] Holmes, P., Lumley, J., and Berkooz, G., *Turbulence, Coherent Structures, Dynamical Systems and Symmetry*, Cambridge Univ. Press, Cambridge, England, U.K., 1996.
- [16] Fox, R. L., and Miura, H., "An Approximate Analysis Technique for Design Calculations," *AIAA Journal*, Vol. 9, No. 1, 1971, pp. 177–179. doi:10.2514/3.6141
- [17] Noor, A., and Peters, J., "Reduced Basis Technique for Nonlinear Analysis of Structures," *AIAA Journal*, Vol. 18, No. 4, 1980, pp. 455–462. doi:10.2514/3.50778
- [18] Afanasiev, K., and Hinze, M., "Adaptive Control of a Wake Flow Using Proper Orthogonal Decomposition," *Lecture Notes in Pure and Applied Mathematics*, Vol. 216, Marcel Dekker, New York, 2001, pp. 317–332.
- [19] Arian, E., Fahl, M., and Sachs, E., "Trust-Region Proper Orthogonal Decomposition for Optimal Flow Control," Inst. for Computer Applications in Science and Engineering, TR ICASE 2000-25, Hampton, VA, May 2000.
- [20] Daniel, L., Siong, O., Chay, L., Lee, K., and White, J., "Multiparameter Moment Matching Model Reduction Approach for Generating Geometrically Parameterized Interconnect Performance Models," *IEEE Transactions on Computer-Aided Design of Integrated Circuits and Systems*, Vol. 23, No. 5, May 2004, pp. 678–693. doi:10.1109/TCAD.2004.826583
- [21] Gunzburger, M., Peterson, J., and Shadid, J., "Reduced-Order Modeling of Time-Dependent PDEs with Multiple Parameters in the Boundary Data," *Computer Methods in Applied Mechanics and Engineering*, Vol. 196, Nos. 4–6, 2007, pp. 1030–1047. doi:10.1016/j.cma.2006.08.004
- [22] Weickum, G., Eldred, M., and Maute, K., "Multi-Point Extended Reduced Order Modeling for Design Optimization and Uncertainty Analysis," 2nd AIAA Multidisciplinary Design Optimization Specialist Conference, AIAA Paper 2006-2145, Newport, RI, May 2006.
- [23] Gugercin, S., Antoulas, A., and Beattie, C., "A Rational Krylov Iteration for Optimal H2 Model Reduction," *Proceedings of the 17th International Symposium on Mathematical Theory of Networks and Systems*, July 2006, pp. 1665–1667.
- [24] Veroy, K., Prud'homme, C., Rovas, D., and Patera, A., "A Posteriori Error Bounds for Reduced-Basis Approximation of Parametrized Noncoercive and Nonlinear Elliptic Partial Differential Equations," Proceedings of the 16th AIAA Computational Fluid Dynamics Conference, AIAA Paper 2003-3847, Orlando, FL, 2003.
- [25] Veroy, K., and Patera, A., "Certified Real-Time Solution of the Parametrized Steady Incompressible Navier-Stokes Equations: Rigorous Reduced-Basis a Posteriori Error Bounds," *International Journal for Numerical Methods in Fluids*, Vol. 47, Nos. 8–9, 2005, pp. 773–788. doi:10.1002/flid.867
- [26] Grepl, M., and Patera, A., "A Posteriori Error Bounds for Reduced-Basis Approximations of Parametrized Parabolic Partial Differential Equations," *ESAIM. Mathematical Modelling and Numerical Analysis*, Vol. 39, No. 1, 2005, pp. 157–181.
- [27] Grepl, M., "Reduced-Basis Approximation and A Posteriori Error Estimation for Parabolic Partial Differential Equations," Ph.D. Thesis, Massachusetts Inst. of Technology, Cambridge, MA, June 2005.

- [28] Cockburn, B., and Shu, C.-W., "Runge-Kutta Discontinuous Galerkin Methods for Convection-Dominated Problems," *Journal of Scientific Computing*, Vol. 16, No. 3, 2001, pp. 173–261. doi:10.1023/A:1012873910884
- [29] Fidkowski, K., and Darmofal, D., "Development of a Higher-Order Solver for Aerodynamic Applications," the 42nd AIAA Aerospace Sciences Meeting and Exhibit, AIAA Paper 2004-0436, Reno, NV, 2004.
- [30] Garzon, V., and Darmofal, D., "Impact of Geometric Variability on Axial Compressor Performance," *Journal of Turbomachinery*, Vol. 125, No. 4, Oct. 2003, pp. 692–703. doi:10.1115/1.1622715
- [31] Lisandrin, P., Carpentieri, G., and Tooren, M., "Investigation over CFD-Based Models for the Identification of Nonlinear Unsteady Aerodynamics Responses," *AIAA Journal*, Vol. 44, No. 9, Sept. 2006, pp. 2043–2050. doi:10.2514/1.18726
- [32] Bui-Thanh, T., Willcox, K., and Ghattas, O., "Model Reduction for Large-Scale Systems with High-Dimensional Parametric Input Space," *SIAM Journal on Scientific Computing* (to be published); also Massachusetts Inst. of Technology, TR ACDL TR-07-2, Cambridge, MA, Aug. 2007.
- [33] Bui-Thanh, T., Willcox, K., Ghattas, O., and van Bloemen Waanders, B., "Goal-Oriented, Model-Constrained Optimization for Reduction of Large-Scale Systems," *Journal of Computational Physics*, Vol. 224, No. 2, June 2007, pp. 880–896. doi:10.1016/j.jcp.2006.10.026
- [34] Akcelik, V., Biros, G., Ghattas, O., Hill, J., Keyes, D., and van Bloemen Waanders, B., "Parallel Algorithms for PDE-Constrained Optimization," *Frontiers of Parallel Computing*, edited by M. Heroux, P. Raghaven, and H. Simon, Society for Industrial and Applied Mathematics, Philadelphia, 2006.
- [35] Branch, M., Coleman, T., and Li, Y., "A Subspace, Interior, and Conjugate Gradient Method for Large-Scale Bound-Constrained Minimization Problems," *SIAM Journal on Scientific Computing*, Vol. 21, No. 1, Oct. 1999, pp. 1–23. doi:10.1137/S1064827595289108
- [36] Nocedal, J., and Wright, S., *Numerical Optimization*, Springer, New York, 1999.
- [37] Eisenstat, S., and Walker, H., "Choosing the Forcing Terms in an Inexact Newton Method," *SIAM Journal on Scientific Computing*, Vol. 17, No. 1, 1996, pp. 16–32. doi:10.1137/0917003
- [38] Castanier, M., Ottarsson, G., and Pierre, C., "A Reduced Order Modeling Technique for Mistuned Bladed Disks," *Journal of Vibration and Acoustics*, Vol. 119, No. 3, 1997, pp. 439–447. doi:10.1115/1.2889743
- [39] Yang, M.-T., and Griffin, J. H., "A Reduced Order Model of Mistuning Using a Subset of Nominal Modes," *Journal of Engineering for Gas Turbines and Power*, Vol. 123, No. 4, 2001, pp. 893–900. doi:10.1115/1.1385197
- [40] Petrov, E., Sanliturk, K., Ewins, D., and Elliott, R., "Quantitative Prediction of the Effects of Mistuning Arrangement on Resonant Response of a Practical Turbine Bladed Disk," *5th National Turbine Engine High Cycle Fatigue Conference*, Chandler, AZ, 2000.
- [41] Feiner, D., and Griffin, J. H., "Mistuning Identification of Bladed Disks Using a Fundamental Mistuning Model. Part 2: Application," *Journal of Turbomachinery*, Vol. 126, No. 1, 2004, pp. 159–165. doi:10.1115/1.1643914
- [42] Lim, S., Castanier, M., and Pierre, C., "Vibration Modeling of Bladed Disks Subject to Geometric Mistuning and Design Changes," 45th AIAA/ASME/ASCE/AHS/ASC Structures, Structural Dynamics and Materials Conference, AIAA Paper 2004-1686, Palm Springs, CA, Apr. 2004.
- [43] Brown, J., Slater, J., and Grandhi, R., "Probabilistic Analysis of Geometric Uncertainty Effects of Blade Modal Response," ASME Turbo Expo, American Society of Mechanical Engineers Paper GT2003-38557, Atlanta, GA, June 2003.
- [44] Sinha, A., Hall, B., Cassenti, B., and Hilbert, G., "Vibratory Parameters of Blades from Coordinate Measurement Machine (CMM) Data," *Proceedings of 9th National Turbine Engine High Cycle Fatigue (HCF) Conference*, Pinehurst, NC, Mar. 2004.
- [45] Davis, T., "Algorithm 832: UMFPACK, an Unsymmetric-Pattern Multifrontal Method," *ACM Transactions on Mathematical Software*, Vol. 30, No. 2, June 2004, pp. 196–199. doi:10.1145/992200.992206
- [46] DeGroot, M., *Probability and Statistics*, Addison Wesley Longman, Reading, MA, 1991.

J. Samareh
Associate Editor